frontiers in Electronic Materials

REVIEW
published: 29 March 2022
doi: 10.3389/femat.2022.869803

Electrical Energy Storage From First Principles

Zhijun Jiang[1,2], Bin Xu[3], Sergey Prosandeev[2], Jorge Íñiguez[4,5], Hongjun Xiang[6,7] and L. Bellaiche[2]**

[1]MOE Key Laboratory for Nonequilibrium Synthesis and Modulation of Condensed Matter, Shaanxi Province Key Laboratory of Advanced Functional Materials and Mesoscopic Physics, School of Physics, Xi'an Jiaotong University, Xi'an, China, [2]Physics Department and Institute for Nanoscience and Engineering, University of Arkansas, Fayetteville, AR, United States, [3]Jiangsu Key Laboratory of Thin Films, School of Physical Science and Technology, Institute of Theoretical and Applied Physics, Soochow University, Suzhou, China, [4]Materials Research and Technology Department, Luxembourg Institute of Science and Technology, Esch/Alzette, Luxembourg, [5]Department of Physics and Materials Science, University of Luxembourg, Esch/Alzette, Luxembourg, [6]Key Laboratory of Computational Physical Sciences (Ministry of Education), State Key Laboratory of Surface Physics, and Department of Physics, Fudan University, Shanghai, China, [7]Shanghai Qi Zhi Institute, Shanghai, China

Dielectric capacitors are particularly suitable to store the electrical energy of a fast-changing nature. Here, we present a review of recent applications of first principles and first-principles-based effective Hamiltonian approaches to the study of energy storage in ferroelectrics, lead-free antiferroelectrics, relaxor ferroelectrics, and nitride semiconductors. Specifically, these approaches are used to investigate the energy density and efficiency in perovskite $BaTiO_3$, $PbTiO_3$, and $KNbO_3$ ferroelectrics; $Bi_{1-x}R_xFeO_3$ antiferroelectric solid solutions (where R is a rare-earth ion); $Ba(Zr,Ti)O_3$ relaxor ferroelectrics; and epitaxial AlN/ScN superlattices. Ultrahigh energy densities and efficiencies are predicted in some of these compounds. In addition, phenomenological models are used to analyze and understand these energy storage results. Consequently, the numerical methods and simple models detailed here can be easily employed to design novel nonlinear dielectrics with further enhanced energy storage performance.

Keywords: energy storage, ferroelectrics, antiferroelectrics, relaxor ferroelectrics, superlattices

OPEN ACCESS

Edited by:
Zhonghua Yao, Wuhan University of Technology, China

Reviewed by:
Shuai Dong, Southeast University, China
Manish Niranjan, Indian Institute of Technology Hyderabad, India

****Correspondence:***
Zhijun Jiang
zjjiang@xjtu.edu.cn
L. Bellaiche
laurent@uark.edu

Specialty section:
This article was submitted to Dielectric Materials, a section of the journal Frontiers in Electronic Materials

Received: *05 February 2022*
Accepted: *21 February 2022*
Published: *29 March 2022*

Citation:
Jiang Z, Xu B, Prosandeev S, Íñiguez J, Xiang H and Bellaiche L (2022) Electrical Energy Storage From First Principles. Front. Electron. Mater. 2:869803. doi: 10.3389/femat.2022.869803

1 INTRODUCTION

Dielectric capacitors with ultrahigh energy density and efficiency are promising for energy storage applications in various electronic applications due to their fast charging/discharging speeds and high stability (Chu et al., 2006; Hao, 2013; Chauhan et al., 2015; Li et al., 2015; Prateek Thakur and Gupta, 2016; Yao et al., 2017; Yang et al., 2019), and intensive efforts have been devoted to improve their relatively low energy densities. For example, dielectric polymers with high dipole density have the potential to achieve ultrahigh energy density with fast discharge and low hysteresis loss (Chu et al., 2006; Li et al., 2015). Recently, antiferroelectrics, relaxor ferroelectrics, and initially nonpolar-based capacitors have been intensively studied because of their low dielectric loss, high polarization, and high breakdown electric field (Peng et al., 2015; Hou et al., 2017; Instan et al., 2017; Pan et al., 2019; Kim et al., 2020; Pan et al., 2021; Wei et al., 2021). For instance, a giant energy density of 154 J/cm^3 with a high efficiency of 97% has been observed in epitaxial lead-free relaxor thin films exhibiting a coexistence of ferroelectric (FE) and anti-FE phases (Peng et al., 2015). A high energy density of 112 J/cm^3 with a high energy efficiency of 80% has also been achieved in lead-free $BiFeO_3$-$BaTiO_3$-$SrTiO_3$ solid solution films (Pan et al., 2019). Ultrahigh energy densities and efficiencies have also been reported in $0.68Pb(Mg_{1/3}Nb_{2/3})O_3$-$0.32PbTiO_3$ (133 J/cm^3 and 75%) and Sm-doped *y*BFO-

$(1-y)$BTO (152 J/cm^3 with a marked enhancement of efficiency above 90%) relaxor ferroelectrics (Kim et al., 2020; Pan et al., 2021). Note that the so-called superparaelectric relaxor ferroelectrics (which exist between the temperature T_m at which the dielectric response exhibits a peak and the Burns temperature T_b) have been demonstrated to possess ultrahigh energy density and efficiency (Pan et al., 2021), which is promising to optimize properties in other relaxor-FE-based systems and nonlinear dielectrics. Other examples include the ultrahigh recoverable energy density in $Ba(Zr_xTi_{1-x})O_3$ relaxor ferroelectric thin films that has been experimentally observed to be 156 J/cm^3 at a high electric field around 3 MV/cm with an efficiency of 72.8% (Instan et al., 2017); and the highest record of energy density up to 307 J/cm^3 with a high efficiency of 89% at 6.6 MV/cm measured in $SrTiO_3$ films grown on an $La_{0.67}Sr_{0.33}MnO_3$ electrode (Hou et al., 2017).

Note that, for nonlinear dielectrics (i.e., ferroelectrics, antiferroelectrics, and relaxors), the stored energy density (U_{st} or W_{st}) is determined by integrating the area between the polarization and the charging curve of the polarization versus electric field (P-E) loop, $U_{st} = \int_0^{P_{max}} EdP$, and the recoverable energy density (U_{rec} or W_{rec}) is determined by the discharging process, $U_{rec} = \int_{Pr}^{P_{max}} EdP$, where P_{max} is the polarization obtained at the maximum applied electric field E_{max} and P_r is the remnant polarization. The efficiency can be defined as $\eta = (U_{rec}/U_{st}) = [U_{rec}/(U_{rec} + U_{loss})] \times 100\%$, where U_{loss} is the energy loss density (Palneedi et al., 2018; Wei et al., 2021). In order to achieve high energy density and efficiency, one can thus imagine a nonlinear type dielectric material to have large polarization (P_{max}) under a high applied electric field (E_{max}) and small hysteresis (with small remnant polarization and energy loss).

The aim of this review article is to discuss the recent first principles and first-principles-based effective Hamiltonian studies aimed at predicting and understanding energy storage in some ferroelectrics (Luo et al., 2016), lead-free antiferroelectrics (Xu et al., 2017), relaxor ferroelectrics (Jiang et al., 2022), and some specific nitride semiconductors (Jiang et al., 2021a).

This article is organized as follows. **Section 2** provides details about the first-principles methods and first-principles-based effective Hamiltonian schemes used for investigating the energy storage properties of these different systems (Luo et al., 2016; Xu et al., 2017; Jiang et al., 2021a; Jiang et al., 2022). **Section 3** reports and discusses energy storage results in ferroelectrics, antiferroelectrics, relaxor ferroelectrics, and nitride semiconductors, from the use of these *ab initio* methods. Finally, **Section 4** provides a summary and perspective on future studies.

2 MATERIALS AND METHODS

2.1 Effective Hamiltonian for $BaTiO_3$, $PbTiO_3$, and $KNbO_3$

The effective Hamiltonian used to study energy storage in some prototypical ferroelectrics (namely, $BaTiO_3$, $PbTiO_3$, and $KNbO_3$) can be expressed as (Nishimatsu et al., 2008; Luo et al., 2016)

$$\begin{aligned} H_{eff} = {} & \frac{M^*_{dipole}}{2}\sum_i \dot{u}_i^2 + \frac{M^*_{acoustic}}{2}\sum_i \dot{w}_i^2 + V^{self}(\{\boldsymbol{u}_i\}) + V^{dpl}(\{\boldsymbol{u}_i\}) \\ & + V^{short}(\{\boldsymbol{u}_i\}) + V^{elas,homo}(\eta_1, \cdots, \eta_6) + V^{elas,inho}(\{\boldsymbol{w}_i\}) \\ & + V^{coup,homo}(\{\boldsymbol{u}_i\}, \eta_1, \cdots, \eta_6) \quad + V^{coup,inho}(\{\boldsymbol{u}_i\}, \{\boldsymbol{w}_i\}) \\ & - Z^* \sum_i E.\boldsymbol{u}_i \end{aligned} \tag{1}$$

where u_i is the local soft-mode amplitude located at the unit cell i, w_i is the local acoustic displacement vector, $\eta_1, \cdots, \eta_6$ represent the component of the homogeneous strain tensor in Voigt notation (Nye, 1985), and M^*_{dipole} and $M^*_{acoustic}$ correspond to the effective masses for local soft modes and acoustic displacements, respectively. The different energies appearing in **Eq. 1** are the two kinetic energies associated with the local soft modes and acoustic displacements, local mode self-energy, long-range dipole–dipole interaction, short-range interactions associated with the local soft modes, elastic energies stemming from homogeneous and inhomogeneous strains, coupling between local soft modes and both homogeneous in inhomogeneous strains, and effect of an external electric field, E.

The effective Hamiltonian parameters for $BaTiO_3$, $PbTiO_3$, and $KNbO_3$ FE systems were determined from first-principles calculations [see details in References (Waghmare and Rabe, 1997; Waghmare et al., 1998; Nishimatsu et al., 2010)].

2.2 Effective Hamiltonian for $Bi_{1-x}Nd_xFeO_3$ Solid Solutions

An effective Hamiltonian (H_{eff}) approach was developed in Refs (Xu et al., 2015; Jiang et al., 2021b) for $Bi_{1-x}Nd_xFeO_3$ (BNFO) solid solutions. The total internal energy E_{int} of this effective Hamiltonian can be expressed as

$$\begin{aligned} E_{int} = {} & E_{BFO}(\{\boldsymbol{u}_i\}, \{\eta_H\}, \{\eta_I\}, \{\boldsymbol{\omega}_i\}, \{\boldsymbol{m}_i\}) + \\ & E_{alloy}(\{\boldsymbol{u}_i\}, \{\boldsymbol{\omega}_i\}, \{\boldsymbol{m}_i\}, \{\eta_{loc}\}) \end{aligned} \tag{2}$$

where E_{BFO} is the effective Hamiltonian of pure $BiFeO_3$ (Kornev et al., 2007), while E_{alloy} represents the effect of substituting Bi by Nd ions in the A sublattice of this perovskite compound. Technically, the effective Hamiltonian of BNFO comprises four different types of degrees of freedom: i) the local soft mode $\{\boldsymbol{u}_i\}$ centered on the A site i (Bi or Nd ion), which is directly related to the local electric dipole moment centered on unit cell i (Zhong et al., 1995); ii) strain tensor that includes the contributions of both homogeneous $\{\eta_H\}$ and inhomogeneous $\{\eta_I\}$ strains; iii) $\{\boldsymbol{\omega}_i\}$ that characterizes the oxygen octahedral tilting about the Fe ion located at the i site of the B sublattice (Kornev et al., 2006); and iv) magnetic moment $\{\boldsymbol{m}_i\}$ centered on the B site of Fe ions (Kornev et al., 2007). Note that a local quantity $\eta_{loc}(i) = \frac{\delta R_{ionic}}{8}\sum_j \sigma_j$ centered on the B site i of Fe ion, where σ_j represents the A sublattice atomic configuration distribution in the BNFO solid solutions and the sum over j runs over the 8 A nearest neighbors of Fe site i; δR_{ionic} represents

the A sublattice relative difference of the ionic radius between the Nd and Bi ions. Note also that one can add to E_{int} an energy contribution given by minus the dot product between polarization and applied electric field, in order to simulate the effect of such a field on physical properties (Xu et al., 2017).

BNFO systems are typically modeled by using 12 × 12 × 12 supercells (containing 8,640 atoms) within this H_{eff} scheme and inside, in which the A site of Bi and Nd ions is randomly distributed. Practically, the total energy of this H_{eff} approach can be used in Monte Carlo (MC) simulations to compute the static properties of BNFO solid solutions at a finite temperature. A total of 20,000 MC sweeps are typically used for equilibration, and an additional 20,000 MC sweeps are employed to compute statistical thermal averages at a finite temperature and an electric field, to obtain converged results (Xu et al., 2017).

2.3 Effective Hamiltonian for Ba(Zr,Ti)O_3 Solid Solutions

The first-principles-based effective Hamiltonian approach has also been recently developed and used to simulate the static and dynamical properties of bulks and films made of Ba(Zr,Ti)O_3 solid solutions (Akbarzadeh et al., 2012; Prosandeev et al., 2013a; Prosandeev et al., 2013b; Wang et al., 2016; Jiang et al., 2017; Jiang et al., 2022). The total internal energy of the effective Hamiltonian in Ba(Zr,Ti)O_3 contains two main terms too:

$$E_{int}\left(\{\boldsymbol{u}_i\},\{\boldsymbol{v}_i\},\eta_H,\{\sigma_j\}\right) = E_{ave}\left(\{\boldsymbol{u}_i\},\{\boldsymbol{v}_i\},\eta_H\right) + E_{loc}\left(\{\boldsymbol{u}_i\},\{\boldsymbol{v}_i\},\{\sigma_j\}\right) \quad (3)$$

where $\{u_i\}$ is the local soft mode in unit cell i (which is proportional to the electric dipole moment centered on the B site of Zr or Ti ions), $\{v_i\}$ are the variables related to the inhomogeneous strain inside cell i, η_H is the homogeneous strain tensor, and $\{\sigma_j\}$ describes the B-sublattice distribution (that is, Zr or Ti ion located at the j site) in the Ba(Zr,Ti)O_3 solid solutions. Note that E_{ave} contains five different contributions: i) the local soft mode self-energy; ii) long-range dipole–dipole interaction; iii) energy as a result of short-range interactions between local soft modes; iv) elastic energy; and v) energy due to the interaction between local soft modes and strains (Zhong et al., 1995). The second energy term E_{loc} describes how the actual distribution of Zr and Ti ions affects the energetics involving the local soft modes u_i and the local strain variables (which depend on the $\{\sigma_j\}$ distribution).

This effective Hamiltonian has been implemented within MC simulations on 12 × 12 × 12 supercells (8,640 atoms), in order to determine and understand energy storage in disordered Ba(Zr,Ti)O_3 (BZT) relaxor ferroelectrics, for the fixed composition of 50% of both Zr and Ti, in both bulks and epitaxial films (Jiang et al., 2022). Note that this H_{eff} successfully predicted the existence of three characteristic temperatures in relaxor ferroelectrics. For instance, for BZT bulks with 50% of Zr and Ti ions, 1) the temperature $T_m \cong$ 130 K, at which the dielectric constant can exhibit a peak (Cross, 1994; Akbarzadeh et al., 2012); 2) the so-called novel critical temperature ($T^* \cong$ 240 K) at which static polar nanoregions (PNRs) typically occur and that has been recently observed in relaxors (Svitelskiy et al., 2005; Dkhil et al., 2009; Akbarzadeh et al., 2012); and 3) Burns temperature ($T_b \cong$ 450 K) that marks the dynamical PNRs at which the finite lifetime of polar fluctuations becomes prominent (Burns and Dacol, 1983; Akbarzadeh et al., 2012).

2.4 First-Principles Calculations for AlN/ScN Superlattices

In Ref. (Jiang et al., 2021a), first-principles calculations were performed on (001) epitaxial 1 × 1 AlN/ScN superlattices within the local density approximation to density functional theory (DFT) and using norm-conserving pseudopotentials (Hamann, 2013), as implemented in the ABINIT package (Gonze et al., 2002). The epitaxial strain can be expressed as $\eta_{in} = (a - a_{eq})/a_{eq}$, where a_{eq} corresponds to the in-plane lattice constant of the equilibrium structure of the nonpolar $P\bar{6}m2$ phase (Jiang et al., 2019a). A 6 × 6 × 4 grid of special k-point and plane-wave kinetic energy cutoff of 50 Hartrees were employed. The effects of dc electric fields applied along the pseudocubic [001] direction on structural properties were taken into account by using finite electric-field methods (Nunes and Vanderbilt, 1994; Nunes and Gonze, 2001; Souza et al., 2002; Zwanziger et al., 2012). The electrical polarization P was computed from the Berry phase approach (King-Smith and Vanderbilt, 1993; Resta, 1994). Note that for each considered strain and magnitude of the applied field, the in-plane lattice vectors were kept fixed while the out-of-plane lattice vector and atomic positions were fully relaxed until all the forces acting on the atoms have a value smaller than 10^{-6} Hartrees/Bohr, in order to mimic epitaxial films being under electric fields.

3 RESULTS AND DISCUSSION

3.1 Energy Storage in Perovskite Ferroelectrics

Let us first present the energy storage results of the prototypical perovskite ferroelectrics $BaTiO_3$, $PbTiO_3$, and $KNbO_3$. A first-principles-based effective Hamiltonian within molecular dynamics simulations was used for these perovskite ferroelectrics and is described in **Section 2.1** and Ref. (Luo et al., 2016).

The temperature dependence of the P-E hysteresis and energy density properties for $BaTiO_3$, $PbTiO_3$, and $KNbO_3$ are shown in **Figure 1**. The energy density of $BaTiO_3$ slowly increases with the temperature below the Curie point at 380 K. In contrast, the energy density rapidly increases with a temperature above the Curie point. Furthermore, the energy density behavior of $KNbO_3$ was numerically found to be very similar to $BaTiO_3$ because of the similarity in the structural phase transition and field-induced phase transition. In the case of $PbTiO_3$, the energy density varies nonmonotonically with the temperature, that is, it first reaches a peak around 820 K and then decreases. This can be explained by the fact that $PbTiO_3$ exhibits a rather weak polarization for temperatures above 820 K. Note that ferroelectrics are not

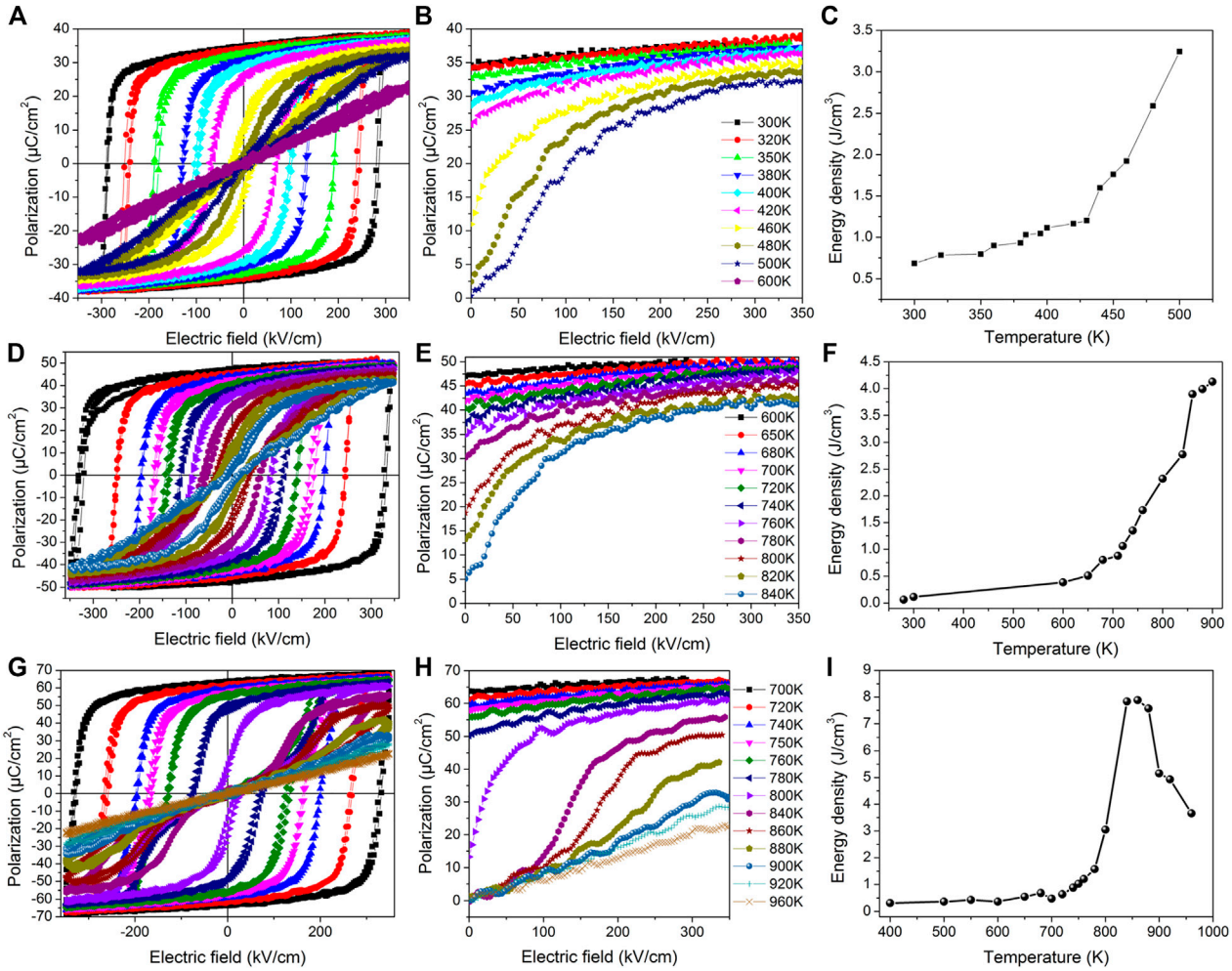

FIGURE 1 | Temperature dependence of hysteresis loops **(A,D,G)**, *P-E* curves **(B,E,H)**, and energy densities **(C,F,I)** in $BaTiO_3$, $KNbO_3$, and $PbTiO_3$. Reproduced from (Luo et al., 2016), with the permission of AIP Publishing.

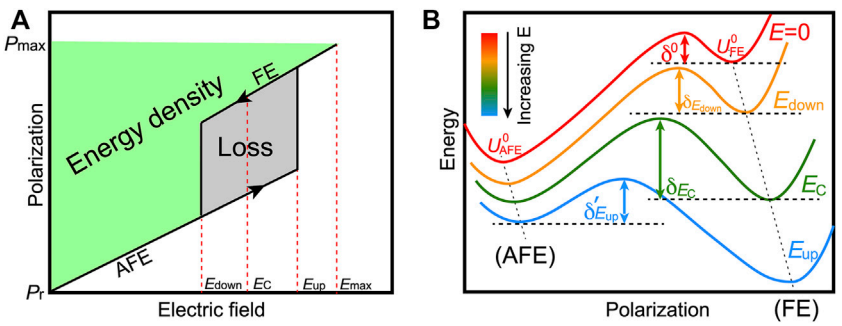

FIGURE 2 | (A) Quantities related to stored energy density and energy loss from the *P-E* double hysteresis loop of antiferroelectrics. The arrows represent the charging and discharging processes. E_{up} and E_{down} describe the critical field at the AFE-FE and FE-AFE phase transitions, respectively. E_C is the field at which the FE and AFE phases have the same energy. **(B)** The energy versus polarization curves with increasing electric field. Reprinted figure with permission from (Xu et al., 2017). Copyright 2017 Springer Nature.

ideal for energy storage applications due to the square shape of their hysteresis loops—which typically gives rise to low energy density and efficiency.

3.2 Energy Storage in Antiferroelectrics

As compared to typical FE systems, antiferroelectric (AFE) materials are very promising for high-power energy storage

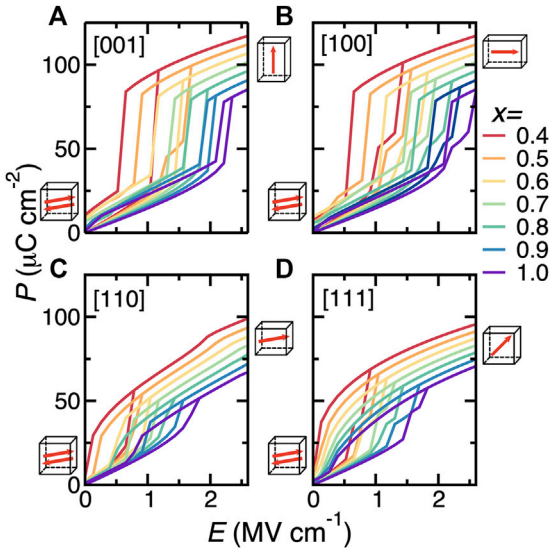

FIGURE 3 | (A–D) *P-E* hysteresis curves at 300 K for electric fields applied along the pseudocubic [001], [100], [110], and [111] directions, respectively, in $Bi_{1-x}Nd_xFeO_3$ solid solutions for Nd composition ranging between 0.4 and 1.0. Reprinted figure with permission from (Xu et al., 2017). Copyright 2017 Springer Nature.

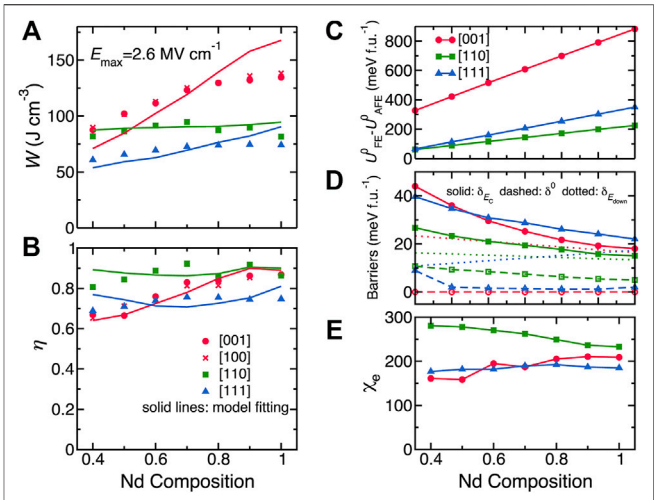

FIGURE 4 | (A,B) Energy density and efficiency in $Bi_{1-x}Nd_xFeO_3$ solid solutions with Nd composition ranging between 0.4 and 1.0 for electric fields applied along the pseudocubic [001], [100], [110], and [111] directions, with the maximum applied electric field being 2.6 MV/cm. The discrete data are calculated from the effective Hamiltonian MC simulations while the solid lines represent the fit of the MC data by the simple model mentioned in the text. **(C–E)** Model parameters *versus* various compositions for different field's orientations. Reprinted figure with permission from (Xu et al., 2017). Copyright 2017 Springer Nature.

applications because of their characteristic *P-E* double hysteresis loops, which is schematized in **Figure 2A** (Xu et al., 2017). There, E_{up} describes the critical field at which the AFE-to-FE transition appears upon charging when increasing field, while E_{down} denotes the critical field for the FE-to-AFE phase transition upon discharging (decreasing field). The green area in **Figure 2A** represents the energy density.

As indicated in **Section 2.2**, a first-principles-based effective Hamiltonian method was employed to investigate the energy storage properties in the rare earth-substituted $BiFeO_3$ multiferroic systems, in general, and disordered BNFO solid solutions, in particular (Xu et al., 2015). This effective Hamiltonian method successfully reproduced the temperature-*versus*-compositional phase diagram of BNFO (Levin et al., 2010; Levin et al., 2011), showing that the *Pnma* phase is the equilibrium structure at room temperature for a moderate level of doping Nd. That is the main reason why BNFO was chosen to investigate energy storage properties at room temperature in Ref. (Xu et al., 2017).

Due to the fact that energy density relies on the applied electric field and polarization, the electric fields considered for BNFO solid solutions have been rescaled by a factor of 1/23, so that the computational *P-E* loop is in good agreement with measurements (Xu et al., 2017). **Figure 3** displays the *P-E* hysteresis curves for four different applied directions of the field (namely, the pseudocubic [001], [100], [110], and [111] directions) for Nd composition changing from 0.4 to 1.0, at room temperature. Note that all the considered compositions adopt the *Pnma* phase at 300 K under zero field. The polarization increases smoothly within the AFE phase under a small electric field and then abruptly jumps up at the AFE-FE phase transition for fields applied along the pseudocubic [001], [100], [110], and [111] directions, respectively.

Let us now focus on the energy density and efficiency, which can be obtained from the *P-E* curves from **Figure 3**. **Figures 4A,B** show the results obtained for different compositions and electric field orientations, using a maximal applied electric field of E_{max} = 2.6 MV/cm. The energy density for fields applied along the [001] direction gives the largest values in magnitude. In contrast, the smallest energy densities in **Figure 4A** correspond to fields applied along the [111] direction. **Figure 4B** further shows that the highest efficiency corresponds to the electric field applied along the [110] direction.

Three compositions (x = 0.5, 0.7, and 1.0) were considered for the electric field applied along the [001] direction, and one composition of x = 0.5 has been selected for the field along the [110] direction in BNFO solid solutions. The energy storage-related results are shown in **Figure 5** [note that the intrinsic breakdown field of E_{max} = 4.37 MV/cm was considered, which is estimated based on an empirical relation (Wang, 2006) that takes into account the experimental band gap of $BiFiO_3$ (Ihlefeld et al., 2008)]. More precisely, the related *P-E* hysteresis curves are shown in **Figure 5A**, while **Figure 5B** displays the energy density of BNFO obtained from the *P-E* hysteresis curves of **Figure 5A**. The energy densities of other experimentally reported materials are shown for comparison and are smaller than that of BNFO systems. The predicted large energy densities (efficiencies) are 164, 191, and 213 J/cm^3 (76%, 88%, and 91%), respectively for x = 0.5, 0.7, and 1, respectively, for the electric field applied along the [001] direction. Similarly, both energy density and efficiency (161 J/cm^3 and 91%) of BNFO with x = 0.5 are very large for the

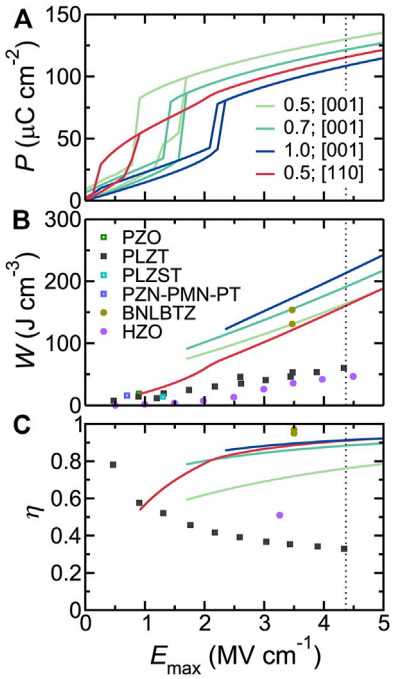

FIGURE 5 | (A) *P-E* hysteresis curves for selected compositions in $Bi_{1-x}Nd_xFeO_3$ solid solutions. **(B)** The energy density as a function of the maximum applied electric field (solid lines). The symbols represent the experimental data from different types of materials. **(C)** The efficiency versus the maximum applied electric field. The dotted vertical line denotes the estimated intrinsic breakdown field for $BiFeO_3$. Reprinted figure with permission from (Xu et al., 2017). Copyright 2017 Springer Nature.

field applied along the [110] direction as well. Note also that BNFO superlattices were not numerically found to have different energy storage properties when compared with disordered BNFO systems. These large energy densities and efficiencies therefore indicate that BNFO systems are promising for energy storage.

In order to understand the energy storage results of **Figure 4**, a simple and general model was proposed for AFE materials, which gives

$$W = P^0_{\mathrm{FE}} E_{\mathrm{down}} + \frac{1}{2}\epsilon_0 \chi_e E^2_{\mathrm{max}} \tag{4}$$

$$\eta = \frac{P^0_{\mathrm{FE}} E_{\mathrm{down}} + \frac{1}{2}\epsilon_0 \chi_e E^2_{\mathrm{max}}}{P^0_{\mathrm{FE}} E_{\mathrm{up}} + \frac{1}{2}\epsilon_0 \chi_e E^2_{\mathrm{max}}} \tag{5}$$

where P^0_{FE} is the polarization of the FE phase along the field's direction as extrapolated to zero field, and χ_e is the dielectric susceptibility for both FE and AFE phases.

Figure 2B shows that the critical field E_C and FE polarization can be expressed in terms of the parameters characterizing the relevant energy landscape of the AFE system, which can be obtained as

$$P^0_{\mathrm{FE}} = \left(U^0_{\mathrm{FE}} - U^0_{\mathrm{AFE}}\right)/E_C \tag{6}$$

The energy difference $U^0_{\mathrm{FE}} - U^0_{\mathrm{AFE}}$ defines the relative stability of the AFE and FE phases, where the superscript corresponds to $E = 0$. We also have

$$E_{\mathrm{down}} = \left(\frac{\delta_{E_{\mathrm{down}}} - \delta^0}{\delta_{E_C} - \delta^0}\right) E_C \tag{7}$$

$$E_{\mathrm{up}} = \left(\frac{2\delta_{E_C} - \delta_{E_{\mathrm{down}}} - \delta^0}{\delta_{E_C} - \delta^0}\right) E_C \tag{8}$$

where δ^0, $\delta_{E_{\mathrm{down}}}$, and δ_{E_C} are the FE-to-AFE barrier at zero field, E_{down}, and E_C, respectively. Consequently, combining **Eqs 4–8** leads to

$$W = \left(\frac{\delta_{E_{\mathrm{down}}} - \delta^0}{\delta_{E_C} - \delta^0}\right)\left(U^0_{\mathrm{FE}} - U^0_{\mathrm{AFE}}\right) + \frac{1}{2}\epsilon_0 \chi_e E^2_{\mathrm{max}} \tag{9}$$

$$\eta = \frac{\left(\frac{\delta_{E_{\mathrm{down}}} - \delta^0}{\delta_{E_C} - \delta^0}\right)\left(U^0_{\mathrm{FE}} - U^0_{\mathrm{AFE}}\right) + \frac{1}{2}\epsilon_0 \chi_e E^2_{\mathrm{max}}}{\left(\frac{2\delta_{E_C} - \delta_{E_{\mathrm{down}}} - \delta^0}{\delta_{E_C} - \delta^0}\right)\left(U^0_{\mathrm{FE}} - U^0_{\mathrm{AFE}}\right) + \frac{1}{2}\epsilon_0 \chi_e E^2_{\mathrm{max}}} \tag{10}$$

Interestingly, the energy density and efficiency data obtained by the effective Hamiltonian MC simulations and shown in **Figures 4A,B** can be well fitted by **Eq. 9** and **Eq. 10**, respectively (the related parameters are shown in **Figures 4C–E**). These good fits of **Figures 4A,B** testify the validity of the aforementioned simple model, which can thus be used to understand and analyze energy storage properties for other AFE materials.

3.3 Energy Storage in Relaxor Ferroelectrics

Relaxor ferroelectrics have also attracted special attention because of their high energy densities and efficiencies, which is highly promising for energy storage applications. Despite the fact that the highest recoverable energy density was achieved in $Ba(Zr_xTi_{1-x})O_3$ relaxor FE thin films at a sustained high electric field of 3.0 MV/cm (Instan et al., 2017), many questions remain to be addressed. For instance, can the first-principles-based effective Hamiltonian method reproduce the experimental finding of ultrahigh energy density in the lead-free relaxor $Ba(Zr_xTi_{1-x})O_3$ system? What will happen if one considers the epitaxial strain on energy storage properties? In particular, could such ultrahigh energy density be understood by a simple phenomenological model? To the best of our knowledge, the effect of the direction of the applied electric field on energy density and efficiency is also presently unknown in $Ba(Zr_xTi_{1-x})O_3$ relaxor ferrolectrics, both in their bulk and epitaxial films.

This section is to answer all these questions by using the first-principles-based effective Hamiltonian approach in $Ba(Zr_{0.5}Ti_{0.5})O_3$ bulk and epitaxial films (Jiang et al., 2022). The effective Hamiltonian is described in **Section 2.3**.

3.3.1 Energy Storage in BZT Bulk

Let us focus on the *P-E* curves in BZT bulk. Note that the simulated electric field is larger than the corresponding experimental one by a factor of 100, which is typical for atomistic effective Hamiltonian simulations (Xu et al., 2017; Jiang et al., 2018) because structural defects are not considered in the theory. A maximum applied field of 3.0 MV/cm was considered, which corresponds to the experimentally applied one in $Ba(Zr_xTi_{1-x})O_3$ thin films (Instan et al., 2017). **Figures**

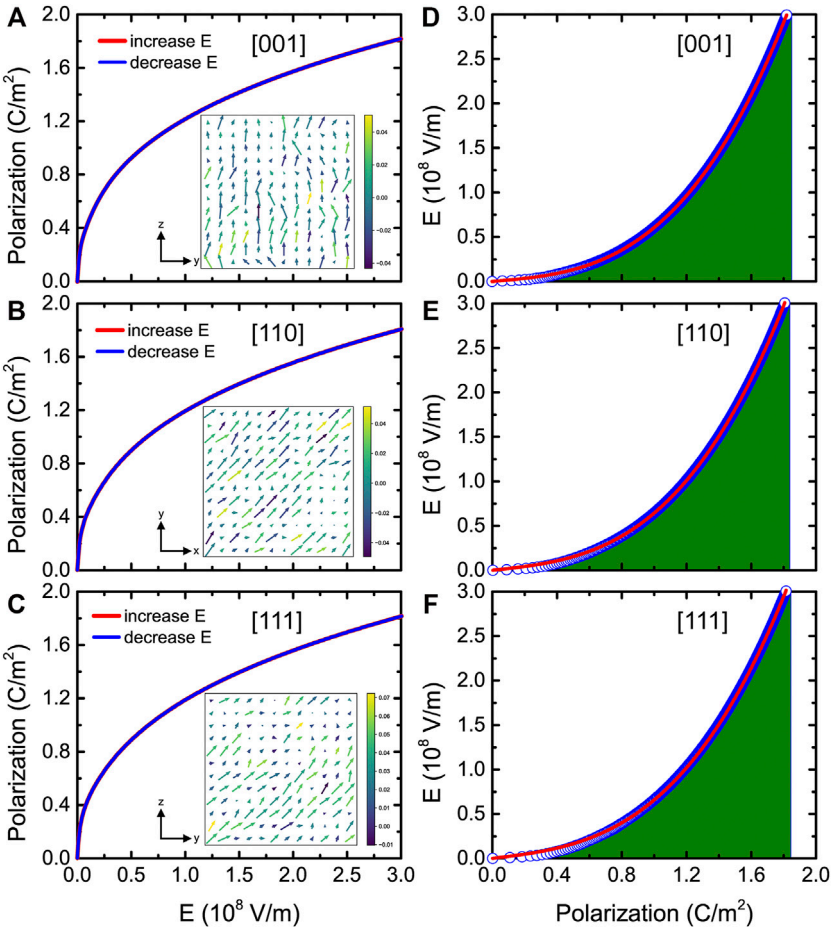

FIGURE 6 | (A–C) *P-E* hysteresis curves at room temperature for fields applied along the pseudocubic [001], [110], and [111] directions, respectively, in BZT bulk. The insets show the dipolar configurations in a given (*y*, *z*) or (*x*, *y*) plane at room temperature for an applied field equal to 0.1 MV/cm. **(D–F)** *E-P* data at room temperature for fields applied along three different directions. The green areas denote the energy densities and the solid red lines denote the fit of the MC data by the phenomenological model. Reprinted figure with permission from (Jiang et al., 2022). Copyright 2022 by the American Physical Society.

6A–C display the polarization versus electric field curves at 300 K for three different fields' directions (namely, electric fields applied along the pseudocubic [001], [110], and [111] directions, respectively) in BZT bulk. An ideal energy efficiency of 100% is predicted due to the complete reversibility of the charging and discharging processes of the *P-E* curves.

The local dipole configurations of **Figures 6A–C** show that the dipoles align along the electric field's applied direction. **Figures 6D–F** display the electric field versus polarization (*E-P*) data for fields applied along the pseudocubic [001], [110], and [111] directions at room temperature, and the green areas represent the energy densities.

The energy density can thus be extracted from the *P-E* or *E-P* data for different temperatures and applied field directions. **Figure 7A** shows that the energy densities linearly increase with temperature for electric fields applied along the [001], [110], and [111] pseudocubic directions. Ultrahigh energy densities are predicted (between 147 and 155 J/cm^3), which agree well with experimental values in $Ba(Zr_xTi_{1-x})O_3$ thin films (Instan et al., 2017).

In order to understand the origin of these energy storage results, a simple Landau-type free energy model was used to describe nonlinear behaviors (Jiang et al., 2021a) and for which, the free energy is given by

$$F = \frac{1}{2}aP^2 + \frac{1}{4}bP^4 - EP \tag{11}$$

where a and b are coefficients of the quadratic and quartic polarization terms, respectively. At equilibrium condition, one must have $\frac{\partial F}{\partial P} = 0$, which thus yields

$$E = aP + bP^3 \tag{12}$$

The numerical *E-P* data for all considered temperatures and field directions were found to be well fitted by **Eq. 12**, which allows to extract the important a and b parameters. **Figures 8A–C** show the related a and b parameters as a function of temperature for electric fields applied along the [001], [110], and [111] directions, respectively, at a maximal

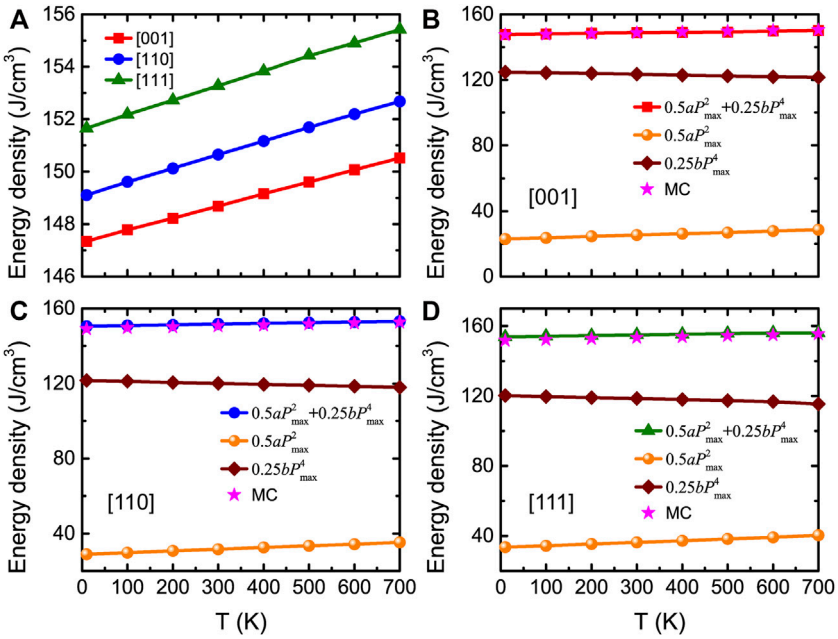

FIGURE 7 | (A) Energy density obtained from MC data as a function of temperature for fields applied along three different directions at E_{max} = 3.0 MV/cm, in BZT bulk. **(B–D)** Total and decomposed energy densities obtained from **Eq. 13** as a function of temperature at E_{max} = 3.0 MV/cm for three different applied field directions, respectively. Stars display the MC data for comparison. Reprinted figure with permission from (Jiang et al., 2022). Copyright 2022 by the American Physical Society.

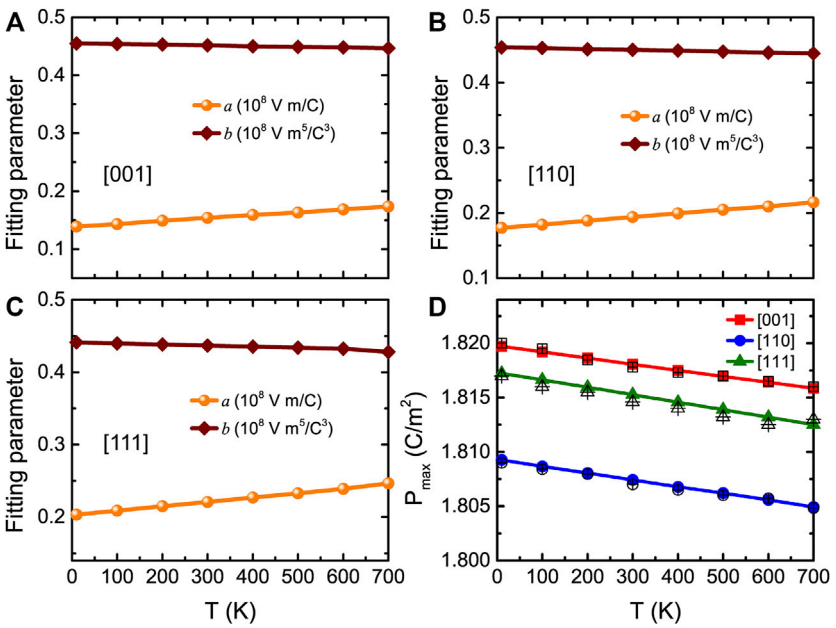

FIGURE 8 | (A–C) Temperature dependence of fitting parameters *a* and *b* for fields applied along three different directions, with a maximal applied electric field being equal to 3.0 MV/cm, in BZT bulk. **(D)** P_{max} obtained from MC simulations (filled symbols) and **Eq. 12** (open symbols) as a function of temperature at E_{max} = 3.0 MV/cm, for fields applied along three different directions in BZT bulk. Reprinted figure with permission from (Jiang et al., 2022). Copyright 2022 by the American Physical Society.

applied electric field equal to 3.0 MV/cm. The *a* parameter linearly increases with temperature, and the *b* parameter only slightly linearly decreases with temperature for the three different field directions. These *a* and *b* coefficients are involved in the expression of the energy density as (Jiang et al., 2021a)

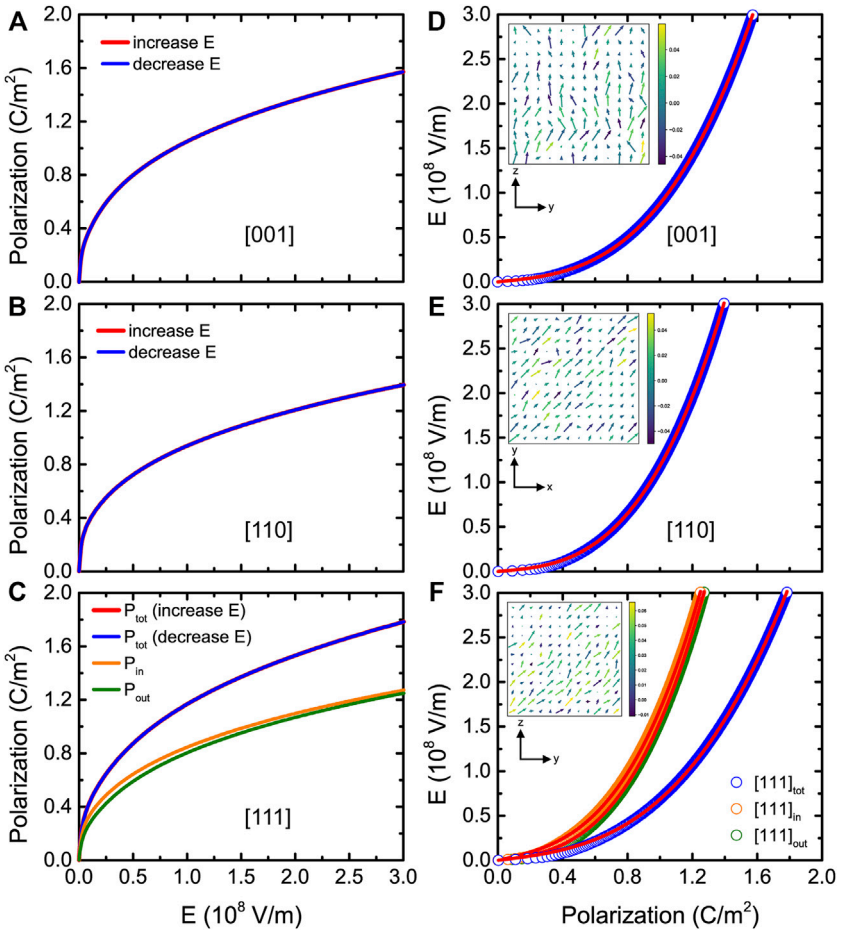

FIGURE 9 | (A-C) *P-E* hysteresis curves at 300 K and 0% strain for fields applied along the pseudocubic [001], [110], and [111] directions, respectively, in (001) BZT films. **(D-F)** *E-P* data at 300 K and 0% strain for fields applied along three different directions. Note that the "in" and "out" notations distinguish between in-plane and out-of-plane components of the polarization when the field is applied along the [111] direction. The insets show the dipolar configurations in a given (y, z) or (x, y) plane at 300 K and 0% strain for an applied field equal to 0.1 MV/cm. Reprinted figure with permission from (Jiang et al., 2022). Copyright 2022 by the American Physical Society.

$$U = \int_0^{P_{\max}} (aP + bP^3)dP = \frac{1}{2}aP_{\max}^2 + \frac{1}{4}bP_{\max}^4 \qquad (13)$$

where $P_{\max}$ is the maximum polarization at the maximal applied electric field of $E_{\max}$. Note that $P_{\max}$ can be obtained from the MC simulations or *via* **Eq. 12** taken at $E_{\max}$. **Figure 8D** shows that both methods give nearly identical results. **Eq. 13** therefore indicates that only a, b, and $P_{\max}$ completely dominate the behaviors and values of the energy density but also tells us that the energy density can be decomposed into two rather simple terms, namely, $\frac{1}{2}aP_{\max}^2$ and $\frac{1}{4}bP_{\max}^4$.

Figures 7B–D show the total and decomposed energy densities calculated from **Eq. 13**, along with the total energy densities obtained from the MC data (with a maximal field of 3.0 MV/cm). One can clearly see that, for any considered temperature, the energy densities obtained from the MC simulations provide nearly identical results than those given by **Eq. 13**.

3.3.2 Energy Storage in (001) BZT Films

Let us now focus on the energy storage performance for (001) BZT films *versus* different epitaxial strains. **Figures 9A–C** display the *P-E* curves at room temperature and zero strain for fields applied along the pseudocubic [001], [110], and [111] directions, respectively. Three types of *P-E* data are shown in **Figure 9C**, which correspond to the [110] in-plane component of the polarization P_{in}, [001] out-of-plane component of the polarization P_{out}, and the total polarization P_{tot}. Moreover, **Figures 9D–F** show the *E-P* data at zero strain and room temperature for fields applied along three different directions, which can be well fitted by **Eq. 12** (solid red lines). **Figure 10A** reports the energy density as a function of strain at 300 K and $E_{\max}$ = 3.0 MV/cm for electric fields applied along the [001],

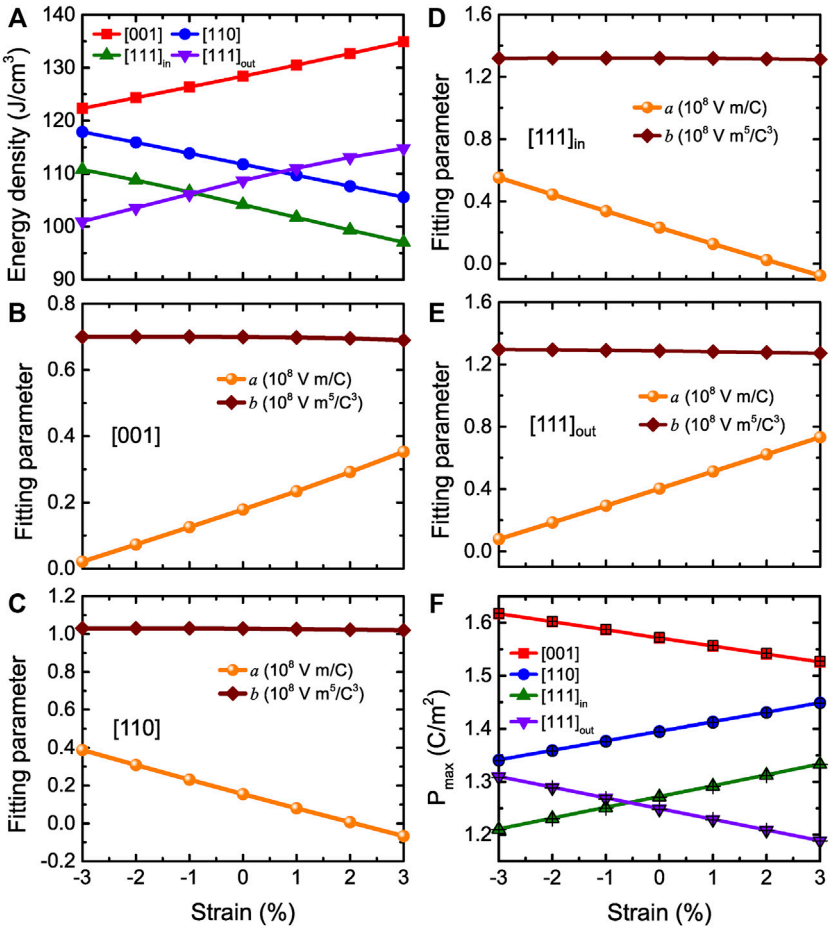

FIGURE 10 | (A) Energy density obtained from MC data as a function of strain at 300 K and E_{max} = 3.0 MV/cm for fields applied three different directions (that is along the [001], [110], and [111] directions, respectively) in BZT films. $[111]_{in}$ versus $[111]_{out}$ components are related to the field applied along [111] direction. **(B,C)** Same as **Figures 8A,B** but as a function of strain at room temperature in BZT films. **(D,E)** display the $[111]_{in}$ (in-plane) and $[111]_{out}$ (out-of-plane) fitting parameters a and b in case of the field applied along the [111] direction, respectively. **(F)** Same as **Figure 8D** but versus strain at room temperature in (001) BZT films. Reprinted figure with permission from (Jiang et al., 2022). Copyright 2022 by the American Physical Society.

[110], and [111] directions, respectively. Note that the $[111]_{in}$ and $[111]_{out}$ notations distinguish between the in-plane and out-of-plane components of the polarization when the field is applied along the [111] direction. **Figure 10A** shows that the energy densities for all considered strains are still large in BZT films (basically larger than 100 J/cm^3).

In order to understand the origin of the energy density results in BZT films, we can also use **Eq. 12** and **Eq. 13**. **Figures 10B–E** display the fitting parameters a and b, while **Figure 10F** shows the P_{max} obtained from both MC simulations and **Eq. 12** at E_{max} as a function of strain. The a parameter linearly increases with strain ranging between −3% and +3%, while P_{max} linearly decreases with strain when fields are applied along the [001] direction. In contrast, the a parameter linearly decreases with strain while P_{max} linearly increases with strain when the field is along the [110] direction. The a parameter and P_{max} related to the in-plane and out-of-plane components for electric fields applied along the [111] direction have the same qualitative behavior as for fields along the [110] and [111] directions, respectively. Note that for all three field directions, the b parameter of **Figures 10B–E** is basically a constant with strain.

The behaviors of a, b, and P_{max} allow us to understand and analyze the results of the energy density in **Figure 10A**. The total and decomposed energy densities obtained from **Eq. 13** are shown in **Figure 11**, where the stars display the MC data for the total energy densities for comparison. **Figure 11A** shows that the first term of $\frac{1}{2}aP_{max}^2$ increases with strain, while the second term $\frac{1}{4}bP_{max}^4$ decreases with strain when the field is applied along the [001] direction. The total energy density for this field direction increases with strain because the change in $\frac{1}{2}aP_{max}^2$ is greater than that of $\frac{1}{4}bP_{max}^4$. In contrast, the energy density behaviors of **Figure 11B** are qualitatively opposite to the [001] case when the field is applied along the [110] direction. **Figures 11C,D** show that the energy density associated with the in-plane and out-of-plane components of the polarization for fields applied along the [111] direction is very similar to the cases of field applied along [110] and [001], respectively. This is because increasing the strain from compressive to tensile energetically

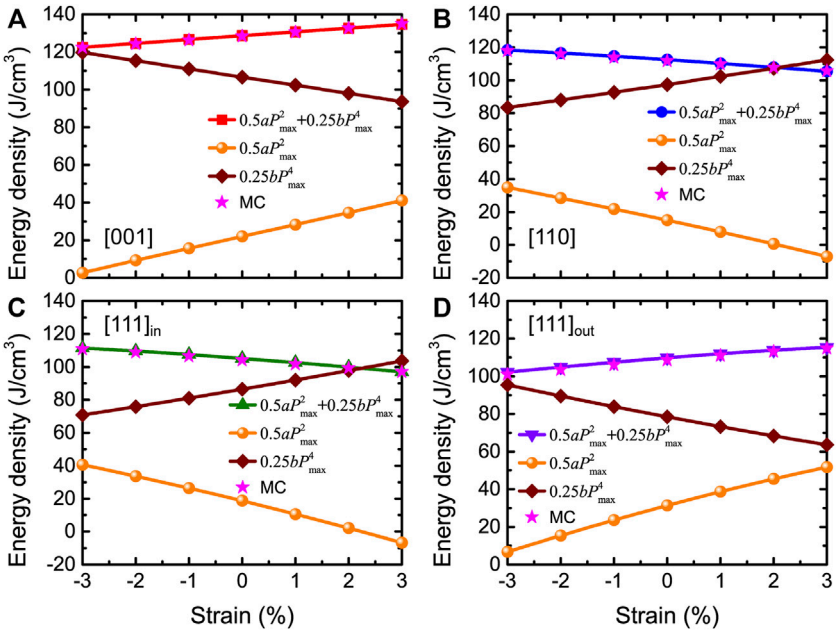

FIGURE 11 | (A–D) Total and decomposed energy densities obtained from **Eq. 13** as a function of strain for fields applied along [001], [110], and [111] (in-plane versus out-of-plane components of the polarization) directions, at E_{max} = 3.0 MV/cm and 300 K in BZT films. Stars display the MC data of **Figure 10A** for comparison. Reprinted figure with permission from (Jiang et al., 2022). Copyright 2022 by the American Physical Society.

disfavors a polarized state having an out-of-plane component while favoring the formation of an in-plane polarization along [110].

3.4 Energy Storage in Epitaxial AlN/ScN Superlattices

In order to improve the energy storage performance, it is timely and important to wonder if there are some multifunctional materials awaiting to be discovered/revealed that have 1) ultrahigh energy storage density; 2) optimal 100% energy efficiency; and 3) giant strain levels when under electric fields. Note that a 100% energy efficiency automatically implies that the transition from the paraelectric/AFE to FE states is fully continuous and reversible. To maximize both energy density and efficiency, one can, for example, imagine a nonlinear dielectric material that exhibits large polarization under feasible high electric fields while being initially in a nonpolar phase at a zero field, and with the charging and discharging processes being completely reversible. The III–V semiconductor-based systems made by mixing AlN and ScN to form $Al_{1-x}Sc_xN$ solid solutions or AlN/ScN superlattices are attractive as these systems can have very large polarization (on the order of 1.0 C/m^2) (Jiang et al., 2019b; Fichtner et al., 2019; Noor-A-Alam et al., 2019; Yasuoka et al., 2020; Yazawa et al., 2021), and an FE phase is energetically close to a nonpolar phase (such that the ground state may be tuned by a physical handle) (Jiang et al., 2019b), which is highly promising for the energy storage performance. The aim of Ref (Jiang et al., 2021a) was to demonstrate that ultrahigh energy storage performance can be achieved in 1 × 1 AlN/ScN superlattices, by using first-principles calculations (the method is described in **Section 2.4**).

Let us now focus on some physical properties of 1 × 1 AlN/ScN superlattices under different epitaxial strains. Previous studies have predicted the existence of different strain-induced regions in 1 × 1 AlN/ScN superlattices (Jiang et al., 2019b), including a wurtzite-derived structure (polar $P3m1$ space group with a polarization along the c-axis) and a hexagonal-derived phase (paraelectric $P\bar{6}m2$ space group). They are related to each other by a continuous change in the internal parameter (u) and the axial ratio (c/a) (Levin et al., 2010). **Figure 12** shows the P-E curves for different compressive strains smaller than −1%, all having the wurtzite-derived structure for ground state (see **Figure 13C** for such structure). A similar information is displayed in **Figure 13A** but for compressive strains and tensile strains larger than −0.5%, which result in a hexagonal-derived ground state (see **Figure 13B** for such phase). The values of the electric fields considered here are the theoretical ones divided by three, in order that the P-E loop of the 1 × 1 AlN/ScN system under a −3% strain becomes very similar to the experimental one corresponding to the $Al_{0.57}Sc_{0.43}N$ film (Fichtner et al., 2019)—as demonstrated in **Figure 12B**. Note that *ab-initio* electric fields are known to be typically larger than their experimental counterparts (Lu et al., 2019; Chen et al., 2019; Jiang et al., 2020). Note also that the polarizations under zero field computed in the 1 × 1 AlN/ScN superlattice experiencing a compressive strain of −3% and the ones measured in the $Al_{0.57}Sc_{0.43}N$ system were found to be very close to each other (see **Figure 12A**), which explains why we decided to determine the renormalization factor of the theoretical fields by comparing the P-E loops of these two compounds.

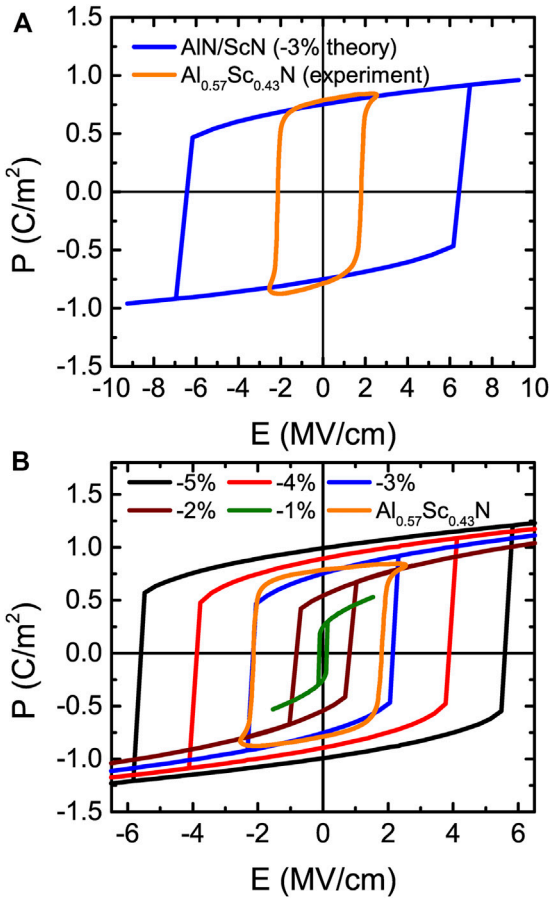

FIGURE 12 | (A) *P-E* loops of 1 × 1 AlN/ScN superlattices for strain at −3% for the actually applied theoretical electric fields and experimentally measured in $Al_{0.57}Sc_{0.43}N$ film. **(B)** *P-E* hysteresis loops for different strains with the ground state being a wurtzite-derived phase in 1 × 1 AlN/ScN superlattices (these electric fields are divided by a factor of 3). Reprinted figure with permission from (Jiang et al., 2021a). Copyright 2021 by the American Physical Society.

Regarding the magnitude of the (renormalized) fields to be considered here, it is first worthwhile to indicate that a recent experiment reported a feasible electric field as high as ~5 MV/cm in $Al_{1-x}Sc_xN$ films (Fichtner et al., 2019). Moreover, one can also estimate the intrinsic breakdown field of such systems *via* the universal expression (Wang, 2006), that is $E_{BI} = 1.36 \times 10^9 \left(\frac{E_g}{4.0}\right)^{\alpha}$ (V/m), where E_g is the band gap, and $\alpha = 1$ for insulators, and $\alpha = 3$ for semiconductors. In such expression, a theoretical corrected band gap of ~3.1 eV is considered for the 1 × 1 AlN/ScN superlattice ground state (Jiang et al., 2019b). An intrinsic breakdown field electric field, E_{break}, of about 6.3 MV/cm is obtained, which is the maximal value of applied electric fields that will be considered below.

Several features are remarkable in **Figure 12B** and **Figure 13A**. First of all, the *P-E* loops of **Figure 12B** are those typical of ferroelectrics with first-order transitions (between two wurtzite-derived structures) for some values of polarization changing of sign under the application of initially opposite electric fields, but with the magnitude of the critical fields of such transitions being very strongly strain dependent. For example, the magnitude of these critical fields is 5.8 MV/cm *versus* 0.2 MV/cm for strains of −5% and −1%, respectively. Such a strong dependency of these fields has also been observed but with respect to the Sc composition in $Al_{1-x}Sc_xN$ solid solutions (Fichtner et al., 2019). Consequently, varying composition in these solid solutions or changing the strain for a fixed alloy or superlattice should yield similar physics and results. Secondly and strikingly, **Figure 13A** reveals a nonlinear behavior of the polarization for small fields (starting from the paraelectric $P\bar{6}m2$ hexagonal-derived phase at a zero field), with the transition between the paraelectric hexagonal-like structure to an FE wurtzite-type phase being continuous and fully reversible upon increasing and decreasing electric fields. Note that such type of continuous and reversible transition has been mentioned in relaxor ferroelectrics (Jiang et al., 2022). As we are going to see, such latter features are indeed promising for applications in electronics and electric power systems. Moreover, larger strain makes the polarization less nonlinear at small fields and also results in a smaller out-of-plane polarization at large fields (**Figure 13A**), which are behaviors that can affect energy storage density (as we also discuss below).

Let us now focus on energy storage properties for the 1 × 1 AlN/ScN superlattices for misfit strains changing from −0.5% to +1%. **Figure 13A** shows that the energy efficiency is 100% because the charging and discharging processes are completely reversible. Regarding the calculated energy density, **Figure 13D** reports it as a function of epitaxial strain ranging between −0.5% and +1%, for electric fields up to two different values, namely, E_{max} = 5 MV/cm, which has been experimentally realized (Fichtner et al., 2019), and E_{break} = 6.3 MV/cm which has been estimated as the intrinsic breakdown field. The energy density can reach very large values, that is, it varies from 127 to 135 J/cm^3 and from 187 to 200 J/cm^3 when using 5 and 6.3 MV/cm for the maximal applied field, respectively. All these large energy densities with the ideal efficiency of 100% thus indicate that the 1 × 1 AlN/ScN superlattices are highly promising for high-power energy storage applications.

To understand these energy storage results of **Figure 13D**, we can also use **Eqs 11–13** to describe the behaviors in initially nonpolar 1 × 1 AlN/ScN superlattices. **Figure 14A** displays the *E-P* data for electric field applied along the pseudocubic [001] direction at a 0.25% strain. The yellow area represents the energy density. The *E-P* data can be well fitted by **Eq. 12** for all the considered strains ranging from −0.5 to +1%.

Figure 14B displays the *a* and *b* fitting parameters versus strain for fields up to the intrinsic breakdown field E_{break} = 6.3 MV/cm. It is worth noting that the *a* parameter linearly increases with strain ranging from −0.5 to +1%. In contrast, the *b* parameter linearly decreases with strain. Note that the change in *a* is much larger in percentage than the change in *b*. **Figure 14C** shows the maximum polarization P_{max} as a function of strain obtained from DFT calculations and the Landau model at E_{max} = 6.3 MV/cm. For all considered strains, the DFT and Landau model provide nearly identical results. In order to understand the results of **Figure 13D** and **Eq. 13** is used to obtain the energy density at E_{max} = 6.3 MV/cm for strain ranging

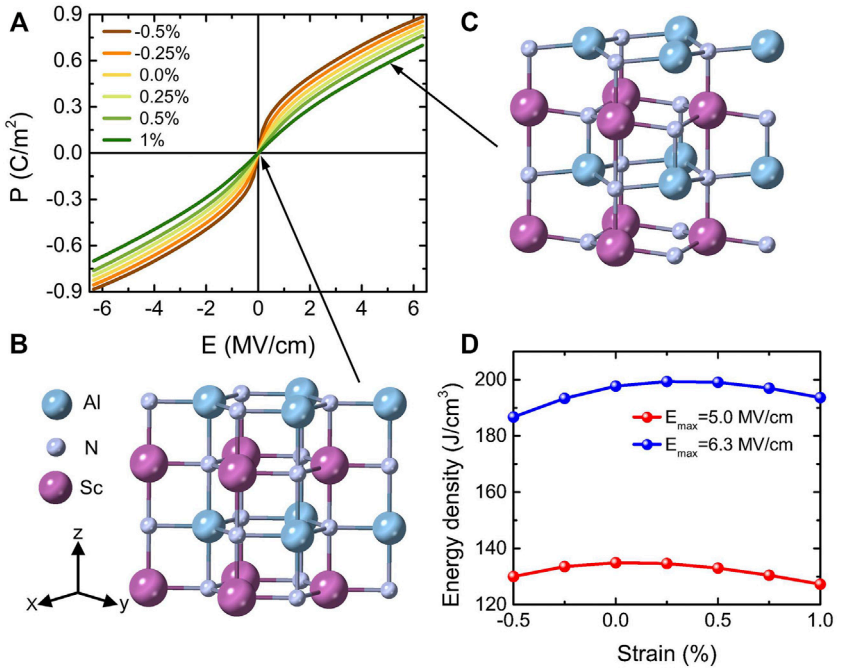

FIGURE 13 | (A) *P-E* hysteresis curves for different strains with the ground state being a hexagonal-derived phase in 1 × 1 AlN/ScN superlattices. **(B,C)** represent the crystal structures of 1% tensile strain under electric fields of 0 and 5 MV/cm, respectively. **(D)** Energy density as a function of strain for two different maximum fields of 5.0 and 6.3 MV/cm. Reprinted figure with permission from (Jiang et al., 2021a). Copyright 2021 by the American Physical Society.

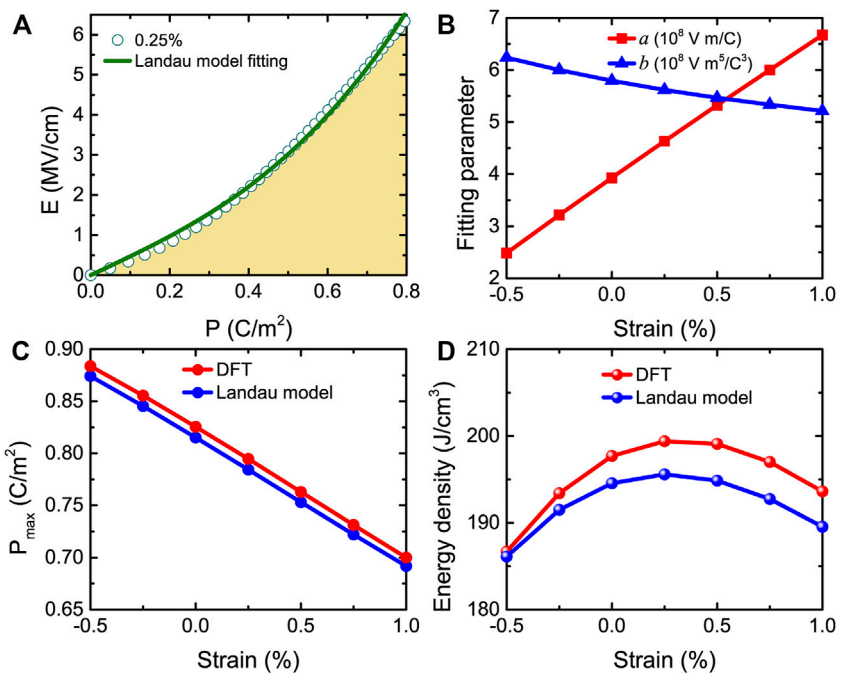

FIGURE 14 | (A) *E-P* data for the strain at 0.25%, with the yellow area showing the energy density (the solid green line represents the fit of the DFT results by **Eq. 12**). **(B)** Evolution with strain of fitting parameters *a* and *b*. **(C,D)** The strain dependence of P_{max} and energy density obtained from DFT and **Eq. 13**. These data correspond to E_{max} = 6.3 MV/cm. Reprinted figure with permission from (Jiang et al., 2021a). Copyright 2021 by the American Physical Society.

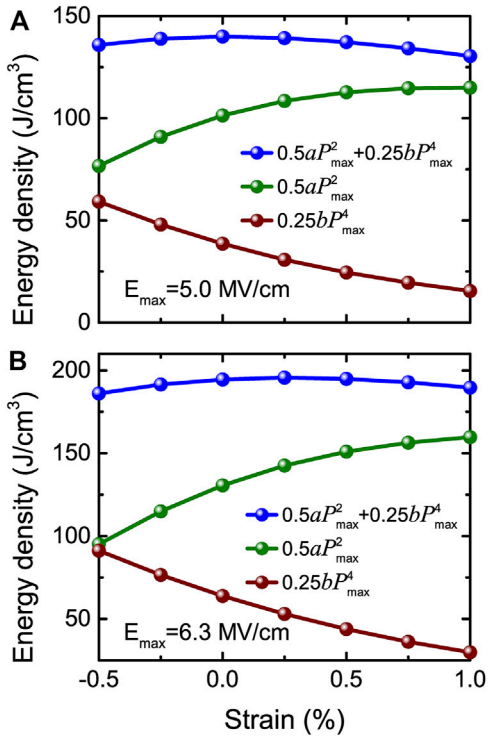

FIGURE 15 | Total and decomposed energy density obtained from **Eq. 13** versus strain at **(A)** E_{max} = 5.0 MV/cm and **(B)** E_{max} = 6.3 MV/cm, respectively. Reprinted figure with permission from (Jiang et al., 2021a). Copyright 2021 by the American Physical Society.

between −0.5 and +1%. **Figure 14D** shows that the Landau model and DFT-obtained energy density behave in a similar qualitative and even quantitative way with the strain, implying that the Landau model can be trusted.

Once again, **Eq. 13** indicates that the energy density can be decomposed into two terms. The first term relies on the product of the fitting a parameter and P^2_{max}, while the second term depends on the product between the b parameter and P^4_{max}. **Figures 15A,B** display the total and decomposed energy densities *versus* strain obtained from **Eq. 13** for two different maximum fields E_{max} = 5.0 and 6.3 MV/cm, respectively. **Figure 15** shows that the Landau model predicted total energy density exhibits a maximum at 0 and 0.25% misfit strain when the largest applied fields are 5.0 and 6.3 MV/cm, respectively. Such numerical findings agree very well with the DFT-obtained results of **Figure 13D**. The strain dependency of $\frac{1}{2}aP^2_{max}$ and $\frac{1}{4}bP^4_{max}$ eventually give rise to a maximum value of the total energy density occurring at different specific strain for each considered maximal electric field.

4 SUMMARY AND PERSPECTIVE

This review summarizes and discusses the energy storage properties in ferroelectrics, lead-free antiferroelectrics, relaxor ferroelectrics, and epitaxial AlN/ScN superlattices using direct first-principles and first-principles-based effective Hamiltonian schemes. Ultrahigh energy densities and efficiencies are predicted in 1) rare-earth substituted $BiFeO_3$ AFE compounds; 2) bulks and films made of the lead-free $Ba(Zr_{0.5}Ti_{0.5})O_3$ relaxor ferroelectrics; and 3) epitaxial AlN/ScN superlattices with initially nonpolar states. Note that an ideal 100% efficiency is predicted in $Ba(Zr_{0.5}Ti_{0.5})O_3$ relaxor ferroelectrics and epitaxial AlN/ScN superlattices due to the second-order character of the field-induced transition toward an FE state. For the studied AFE materials, a simple phenomenological model was proposed to describe the energy density and efficiency, which should be useful in the search for other high energy storage performance in other antiferroelectrics. Another simple Landau model was developed to analyze and understand the energy storage results in BZT relaxor ferroelectrics and epitaxial AlN/ScN superlattices, which reproduces very well the numerical results. The proposed Landau model can also be easily employed for other relaxor ferroelectrics and nonlinear dielectrics, providing insight that there is a trade-off to maximize the energy density: the system should neither be too close nor too far from an FE phase transition.

Note also that one very recent work using high-throughput second-principles calculations (Aramberri et al., 2020) indicated that FE/paraelectric superlattices can be promising for energy storage as well. Other systems can also be investigated by first-principles-based effective Hamiltonian methods, or other *ab initio* techniques, in the near future for energy storage. Examples include the prototypical relaxor ferroelectrics $Pb(Mg_{1/3}Nb_{2/3})O_3$ and $Pb(Mg_{1/3}Nb_{2/3})O_3$-$PbTiO_3$, and $(Bi,R)FeO_3$ antiferroelectrics with R being a rare-earth species different from Nd. We thus hope that this review is useful to the scientific community and deepens the field of energy storage.

AUTHOR CONTRIBUTIONS

ZJ wrote the original manuscript. LB supervised the study. BX, SP, JÍ, HX and LB revised the manuscript. All authors contributed to the interpretation of the results.

FUNDING

This work is supported by the National Natural Science Foundation of China (Grant No. 11804138), Shandong Provincial Natural Science Foundation (Grant No. ZR2019QA008), and "Young Talent Support Plan" of Xi'an Jiaotong University (Grant No. WL6J004). BX acknowledges financial support from National Natural Science Foundation of China under Grant No. 12074277 and Natural Science Foundation of Jiangsu Province (BK20201404), the startup fund from Soochow University, and the support from Priority Academic Program Development (PAPD) of Jiangsu Higher Education Institutions. JÍ acknowledges funding from the Luxembourg National Research Fund through the CORE program (Grant No. FNR/C18/MS/12705883 REFOX, JÍ). HX is supported by the National Natural

Science Foundation of China (Grants No. 11825403 and 11991061). SP and LB acknowledge the Office of Naval Research for the support under Grant No. N00014-21-1-2086. LB also acknowledges the Vannevar Bush Faculty Fellowship Grant No. N00014-20-1-2834 from the Department of Defense and the ARO Grant No. W911NF-21-1-0113.

REFERENCES

Akbarzadeh, A. R., Prosandeev, S., Walter, E. J., Al-Barakaty, A., and Bellaiche, L. (2012). Finite-Temperature Properties of $Ba(Zr,Ti)O_3$ Relaxors from First Principles. *Phys. Rev. Lett.* 108, 257601. doi:10.1103/physrevlett.108.257601

Aramberri, H., Fedorova, N. S., and Íñiguez, J. (2020) Ferroelectric/paraelectric Superlattices for Energy Storage, arXiv:2112.00745.

Burns, G., and Dacol, F. H. (1983). Crystalline Ferroelectrics with Glassy Polarization Behavior. *Phys. Rev. B* 28, 2527–2530. doi:10.1103/physrevb.28.2527

Chauhan, A., Patel, S., Vaish, R., and Bowen, C. (2015). Anti-Ferroelectric Ceramics for High Energy Density Capacitors. *Materials* 8, 8009–8031. doi:10.3390/ma8125439

Chen, L., Xu, C., Tian, H., Xiang, H., Íñiguez, J., Yang, Y., et al. (2019). Electric-Field Control of Magnetization, Jahn-Teller Distortion, and Orbital Ordering in Ferroelectric Ferromagnets. *Phys. Rev. Lett.* 122, 247701. doi:10.1103/physrevlett.122.247701

Chu, B., Zhou, X., Ren, K., Neese, B., Lin, M., Wang, Q., et al. (2006). A Dielectric Polymer with High Electric Energy Density and Fast Discharge Speed. *Science* 313, 334–336. doi:10.1126/science.1127798

Cross, L. E. (1994). Relaxorferroelectrics: An Overview. *Ferroelectrics* 151, 305–320. doi:10.1080/00150199408244755

Dkhil, B., Gemeiner, P., Al-Barakaty, A., Bellaiche, L., Dul'kin, E., Mojaev, E., et al. (2009). Intermediate Temperature Scale T^* in lead-based Relaxor Systems. *Phys. Rev. B* 80, 064103. doi:10.1103/physrevb.80.064103

Fichtner, S., Wolff, N., Lofink, F., Kienle, L., and Wagner, B. (2019). AlScN: A III-V Semiconductor Based Ferroelectric. *J. Appl. Phys.* 125, 114103. doi:10.1063/1.5084945

Gonze, X., Beuken, J.-M., Caracas, R., Detraux, F., Fuchs, M., Rignanese, G.-M., et al. (2002). First-principles Computation of Material Properties: the ABINIT Software Project. *Comput. Mater. Sci.* 25, 478–492. doi:10.1016/s0927-0256(02)00325-7

Hamann, D. R. (2013). Optimized Norm-Conserving Vanderbilt Pseudopotentials. *Phys. Rev. B* 88, 085117. doi:10.1103/physrevb.88.085117

Hao, X. (2013). A Review on the Dielectric Materials for High Energy-Storage Application. *J. Adv. Dielect.* 03, 1330001. doi:10.1142/s2010135x13300016

Hou, C., Huang, W., Zhao, W., Zhang, D., Yin, Y., and Li, X. (2017). Ultrahigh Energy Density in $SrTiO_3$ Film Capacitors. *ACS Appl. Mater. Inter.* 9, 20484–20490. doi:10.1021/acsami.7b02225

Ihlefeld, J. F., Podraza, N. J., Liu, Z. K., Rai, R. C., Xu, X., Heeg, T., et al. (2008). Optical Band gap of $BiFeO_3$ Grown by Molecular-Beam Epitaxy. *Appl. Phys. Lett.* 92, 142908. doi:10.1063/1.2901160

Instan, A. A., Pavunny, S. P., Bhattarai, M. K., and Katiyar, R. S. (2017). Ultrahigh Capacitive Energy Storage in Highly Oriented $Ba(Zr_xTi_{1-x})O_3$ Thin Films Prepared by Pulsed Laser Deposition. *Appl. Phys. Lett.* 111, 142903. doi:10.1063/1.4986238

Jiang, Z., Paillard, C., Vanderbilt, D., Xiang, H., and Bellaiche, L. (2019). Designing Multifunctionality via Assembling Dissimilar Materials: Epitaxial AlN/ScN Superlattices. *Phys. Rev. Lett.* 123, 096801. doi:10.1103/PhysRevLett.123.096801

Jiang, Z., Paillard, C., Xiang, H., and Bellaiche, L. (2020). Linear versus Nonlinear Electro-Optic Effects in Materials. *Phys. Rev. Lett.* 125, 017401. doi:10.1103/PhysRevLett.125.017401

Jiang, Z., Nahas, Y., Prokhorenko, S., Prosandeev, S., Wang, D., Íñiguez, J., et al. (2018). Giant Electrocaloric Response in the Prototypical $Pb(Mg,Nb)O_3$ Relaxor Ferroelectric from Atomistic Simulations. *Phys. Rev. B* 97, 104110. doi:10.1103/physrevb.97.104110

Jiang, Z., Prokhorenko, S., Prosandeev, S., Nahas, Y., Wang, D., Íñiguez, J., et al. (2017). Electrocaloric Effects in the lead-free $Ba(Zr,Ti)O_3$ Relaxor Ferroelectric from Atomistic Simulations. *Phys. Rev. B* 96, 014114. doi:10.1103/physrevb.96.014114

Jiang, Z., Prosandeev, S., and Bellaiche, L. (2022). Energy Storage in lead-free $Ba(Zr,Ti)O_3$ Relaxor Ferroelectrics: Large Densities and Efficiencies and Their Origins. *Phys. Rev. B* 105, 024102. doi:10.1103/physrevb.105.024102

Jiang, Z., Xu, B., Prosandeev, S., Nahas, Y., Prokhorenko, S., Íñiguez, J., et al. (2021). Electrocaloric Effects in Multiferroics. *Phys. Rev. B* 103, L100102. doi:10.1103/physrevb.103.l100102

Jiang, Z., Xu, B., Xiang, H., and Bellaiche, L. (2021). Ultrahigh Energy Storage Density in Epitaxial AlN/ScN Superlattices. *Phys. Rev. Mater.* 5, L072401. doi:10.1103/physrevmaterials.5.l072401

Kim, J., Saremi, S., Acharya, M., Velarde, G., Parsonnet, E., Donahue, P., et al. (2020). Ultrahigh Capacitive Energy Density in Ion-Bombarded Relaxor Ferroelectric Films. *Science* 369, 81–84. doi:10.1126/science.abb0631

King-Smith, R. D., and Vanderbilt, D. (1993). Theory of Polarization of Crystalline Solids. *Phys. Rev. B* 47 (R), 1651–1654. doi:10.1103/physrevb.47.1651

Kornev, I. A., Bellaiche, L., Janolin, P.-E., Dkhil, B., and Suard, E. (2006). Phase Diagram of $Pb(Zr,Ti)O_3$ Solid Solutions from First Principles. *Phys. Rev. Lett.* 97, 157601. doi:10.1103/physrevlett.97.157601

Kornev, I. A., Lisenkov, S., Haumont, R., Dkhil, B., and Bellaiche, L. (2007). Finite-Temperature Properties of Multiferroic $BiFeO_3$. *Phys. Rev. Lett.* 99, 227602. doi:10.1103/physrevlett.99.227602

Levin, I., Karimi, S., Provenzano, V., Dennis, C. L., Wu, H., Comyn, T. P., et al. (2010). Reorientation of Magnetic Dipoles at the Antiferroelectric-Paraelectric Phase Transition of $Bi_{1-x}Nd_xFeO_3$ ($0.15 \leq x \leq 0.25$). *Phys. Rev. B* 81, 020103(R). doi:10.1103/physrevb.81.020103

Levin, I., Tucker, M. G., Wu, H., Provenzano, V., Dennis, C. L., Karimi, S., et al. (2011). Displacive Phase Transitions and Magnetic Structures in Nd-Substituted $BiFeO_3$. *Chem. Mater.* 23, 2166–2175. doi:10.1021/cm1036925

Li, Q., Chen, L., Gadinski, M. R., Zhang, S., Zhang, G., Li, H. U., et al. (2015). Flexible High-Temperature Dielectric Materials from Polymer Nanocomposites. *Nature* 523, 576–579. doi:10.1038/nature14647

Lu, J., Chen, G., Luo, W., Íñiguez, J., Bellaiche, L., and Xiang, H. (2019). Ferroelectricity with Asymmetric Hysteresis in Metallic LiO_sO_3 Ultrathin Films. *Phys. Rev. Lett.* 122, 227601. doi:10.1103/physrevlett.122.227601

Luo, B., Wang, X., Tian, E., Wu, L., and Li, L. (2016). First-principles Effective Hamiltonian Simulation of ABO_3-type Perovskite Ferroelectrics for Energy Storage Application. *J. Appl. Phys.* 120, 074106. doi:10.1063/1.4961204

Nishimatsu, T., Iwamoto, M., Kawazoe, Y., and Waghmare, U. V. (2010). First-principles Accurate Total Energy Surfaces for Polar Structural Distortions of $BaTiO_3$, $PbTiO_3$, and $SrTiO_3$: Consequences for Structural Transition Temperatures. *Phys. Rev. B* 82, 134106. doi:10.1103/physrevb.82.134106

Nishimatsu, T., Waghmare, U. V., Kawazoe, Y., and Vanderbilt, D. (2008). Fast Molecular-Dynamics Simulation for Ferroelectric Thin-Film Capacitors Using a First-Principles Effective Hamiltonian. *Phys. Rev. B* 78, 104104. doi:10.1103/physrevb.78.104104

Noor-A-Alam, M., Z. Olszewski, O., and Nolan, M. (2019). Ferroelectricity and Large Piezoelectric Response of AlN/ScN Superlattice. *ACS Appl. Mater. Inter.* 11, 20482–20490. doi:10.1021/acsami.8b22602

Nunes, R. W., and Gonze, X. (2001). Berry-phase Treatment of the Homogeneous Electric Field Perturbation in Insulators. *Phys. Rev. B* 63, 155107. doi:10.1103/physrevb.63.155107

Nunes, R. W., and Vanderbilt, D. (1994). Real-Space Approach to Calculation of Electric Polarization and Dielectric Constants. *Phys. Rev. Lett.* 73, 712–715. doi:10.1103/physrevlett.73.712

Nye, J. F. (1985). *Physical Properties of Crystals: Their Representation by Tensors and Matrices*. Oxford: Oxford University Press.

Palneedi, H., Peddigari, M., Hwang, G.-T., Jeong, D.-Y., and Ryu, J. (2018). High-performance Dielectric Ceramic Films for Energy Storage Capacitors: Progress and Outlook. *Adv. Funct. Mater.* 28, 1803665. doi:10.1002/adfm.201803665

Pan, H., Lan, S., Xu, S., Zhang, Q., Yao, H., Liu, Y., et al. (2021). Ultrahigh Energy Storage in Superparaelectric Relaxor Ferroelectrics. *Science* 374, 100–104. doi:10.1126/science.abi7687

Pan, H., Li, F., Liu, Y., Zhang, Q., Wang, M., Lan, S., et al. (2019). Ultrahigh-energy Density lead-free Dielectric Films via Polymorphic Nanodomain Design. *Science* 365, 578–582. doi:10.1126/science.aaw8109

Peng, B., Zhang, Q., Li, X., Sun, T., Fan, H., Ke, S., et al. (2015). Giant Electric Energy Density in Epitaxial lead-free Thin Films with Coexistence of

Ferroelectrics and Antiferroelectrics. *Adv. Electron. Mater.* 1, 1500052. doi:10.1002/aelm.201500052

Prateek Thakur, V. K., and Gupta, R. K. (2016). Recent Progress on Ferroelectric Polymer-Based Nanocomposites for High Energy Density Capacitors: Synthesis, Dielectric Properties, and Future Aspects. *Chem. Rev.* 116, 4260–4317. doi:10.1021/acs.chemrev.5b00495

Prosandeev, S., Wang, D., Akbarzadeh, A. R., Dkhil, B., and Bellaiche, L. (2013). Field-Induced Percolation of Polar Nanoregions in Relaxor Ferroelectrics. *Phys. Rev. Lett.* 110, 207601. doi:10.1103/physrevlett.110.207601

Prosandeev, S., Wang, D., and Bellaiche, L. (2013). Properties of Epitaxial Films Made of Relaxor Ferroelectrics. *Phys. Rev. Lett.* 111, 247602. doi:10.1103/physrevlett.111.247602

Resta, R. (1994). Macroscopic Polarization in Crystalline Dielectrics: the Geometric Phase Approach. *Rev. Mod. Phys.* 66, 899–915. doi:10.1103/revmodphys.66.899

Souza, I., Íñiguez, J., and Vanderbilt, D. (2002). First-Principles Approach to Insulators in Finite Electric Fields. *Phys. Rev. Lett.* 89, 117602. doi:10.1103/physrevlett.89.117602

Svitelskiy, O., La-Orauttapong, D., Toulouse, J., Chen, W., and Ye, Z.-G. (2005). $PbTiO_3$ addition and Internal Dynamics in $Pb(Zn_{1/3}Nb_{2/3})O_3$ Crystal Studied by Raman Spectroscopy. *Phys. Rev. B* 72, 172106. doi:10.1103/physrevb.72.172106

Waghmare, U. V., and Rabe, K. M. (1997). Ab Initio statistical Mechanics of the Ferroelectric Phase Transition in $PbTiO_3$. *Phys. Rev. B* 55, 6161–6173. doi:10.1103/physrevb.55.6161

Waghmare, U. V., Rabe, K. M., Krakauer, H., Yu, R., and Wang, C.-Z. (1998). Effective Hamiltonian for the Ferroelectric Phase Transitions in $KNbO_3$. *AIP Conf. Proc.* 436, 32.

Wang, D., Bokov, A. A., Ye, Z.-G., Hlinka, J., and Bellaiche, L. (2016). Subterahertz Dielectric Relaxation in lead-free $Ba(Zr,Ti)O_3$ Relaxor Ferroelectrics. *Nat. Commun.* 7, 11014. doi:10.1038/ncomms11014

Wang, L.-M. (2006). "Relationship between Intrinsic Breakdown Field and Bandgap of Materials," in *25th International Conference on Microelectronics* (Belgrade: IEEE), 576–579.

Wei, X.-K., Dunin-Borkowski, R. E., and Mayer, J. (2021). Structural Phase Transition and *In-Situ* Energy Storage Pathway in Nonpolar Materials: A Review. *Materials* 14, 7854. doi:10.3390/ma14247854

Xu, B., Íñiguez, J., and Bellaiche, L. (2017). Designing lead-free Antiferroelectrics for Energy Storage. *Nat. Commun.* 8, 15682. doi:10.1038/ncomms15682

Xu, B., Wang, D., Íñiguez, J., and Bellaiche, L. (2015). Finite-Temperature Properties of Rare-Earth-Substituted $BiFeO_3$ Multiferroic Solid Solutions. *Adv. Funct. Mater.* 25, 552–558. doi:10.1002/adfm.201403811

Yang, L., Kong, X., Li, F., Hao, H., Cheng, Z., Liu, H., et al. (2019). Perovskite lead-free Dielectrics for Energy Storage Applications. *Prog. Mater. Sci.* 102, 72–108. doi:10.1016/j.pmatsci.2018.12.005

Yao, Z., Song, Z., Hao, H., Yu, Z., Cao, M., Zhang, S., et al. (2017). Homogeneous/Inhomogeneous-Structured Dielectrics and Their Energy-Storage Performances. *Adv. Mater.* 29, 1601727. doi:10.1002/adma.201601727

Yasuoka, S., Shimizu, T., Tateyama, A., Uehara, M., Yamada, H., Akiyama, M., et al. (2020). Effects of Deposition Conditions on the Ferroelectric Properties of $(Al_{1-x}Sc_x)N$ Thin Films. *J. Appl. Phys.* 128, 114103. doi:10.1063/5.0015281

Yazawa, K., Drury, D., Zakutayev, A., and Brennecka, G. L. (2021). Reduced Coercive Field in Epitaxial Thin Film of Ferroelectric Wurtzite $Al_{0.7}Sc_{0.3}N$. *Appl. Phys. Lett.* 118, 162903. doi:10.1063/5.0043613

Zhong, W., Vanderbilt, D., and Rabe, K. M. (1995). First-principles Theory of Ferroelectric Phase Transitions for Perovskites: The Case of $BaTiO_3$. *Phys. Rev. B* 52, 6301–6312. doi:10.1103/physrevb.52.6301

Zwanziger, J. W., Galbraith, J., Kipouros, Y., Torrent, M., Giantomassi, M., and Gonze, X. (2012). Finite Homogeneous Electric fields in the Projector Augmented Wave Formalism: Applications to Linear and Nonlinear Response. *Comput. Mater. Sci.* 58, 113–118. doi:10.1016/j.commatsci.2012.01.028

Conflict of Interest: The authors declare that the research was conducted in the absence of any commercial or financial relationships that could be construed as a potential conflict of interest.

Publisher's Note: All claims expressed in this article are solely those of the authors and do not necessarily represent those of their affiliated organizations, or those of the publisher, the editors and the reviewers. Any product that may be evaluated in this article, or claim that may be made by its manufacturer, is not guaranteed or endorsed by the publisher.

Copyright © 2022 Jiang, Xu, Prosandeev, Íñiguez, Xiang and Bellaiche. This is an open-access article distributed under the terms of the Creative Commons Attribution License (CC BY). The use, distribution or reproduction in other forums is permitted, provided the original author(s) and the copyright owner(s) are credited and that the original publication in this journal is cited, in accordance with accepted academic practice. No use, distribution or reproduction is permitted which does not comply with these terms.